SEMICONDUCTORS

10.1126/sciadv.1600069

Van der Waals metal-semiconductor junction: Weak Fermi level pinning enables effective tuning of Schottky barrier

Yuanyue Liu,[1]*† Paul Stradins,[1] Su-Huai Wei[1,2]*

Two-dimensional (2D) semiconductors have shown great potential for electronic and optoelectronic applications. However, their development is limited by a large Schottky barrier (SB) at the metal-semiconductor junction (MSJ), which is difficult to tune by using conventional metals because of the effect of strong Fermi level pinning (FLP). We show that this problem can be overcome by using 2D metals, which are bounded with 2D semiconductors through van der Waals (vdW) interactions. This success relies on a weak FLP at the vdW MSJ, which is attributed to the suppression of metal-induced gap states. Consequently, the SB becomes tunable and can vanish with proper 2D metals (for example, *H*-NbS_2). This work not only offers new insights into the fundamental properties of heterojunctions but also uncovers the great potential of 2D metals for device applications.

INTRODUCTION

Metal-semiconductor junction (MSJ) is a critical component in electronic and optoelectronic devices. One of the most important parameters for the MSJ is the Schottky barrier (SB) height (Φ), an energy barrier height for charge carrier transport across the junction, which has a significant impact on device performance (*1*, *2*). The importance of tuning Φ has recently been emphasized in devices based on two-dimensional (2D) semiconducting transition metal dichalcogenides (MX_2, where M = Mo or W, and X = S, Se, or Te), which have attracted intense interest because of their unique properties and promising applications (*3*–*5*). Tuning Φ could enable a variety of improvements, such as reducing contact resistance, modulating carrier polarity in the channel for transistors, and enhancing selectivity of carrier extraction for photovoltaic cells. The first one is of particular importance in matching the performance with Si or III-V device analogs (*6*, *7*).

However, it is rather difficult to tune Φ for 2D MX_2 by using different common metals because of the effect of Fermi level pinning (FLP). The reason is that Φ is generally determined by the energy difference between the Fermi level (FL) and the semiconductor band edges in the junction

$$\Phi_e = E_{CBM} - E_F \text{ and } \Phi_h = E_F - E_{VBM} \quad (1)$$

where Φ_e and Φ_h are the barrier heights for electrons and holes, respectively, E_F is the Fermi energy, and E_{VBM} and E_{CBM} are the energy of the valence band maximum (VBM) and conduction band minimum (CBM), respectively, of the semiconductor in the junction. Neglecting the metal-semiconductor interaction, Φ should ideally follow the predictions of the Schottky-Mott model

$$\Phi_e = W - E_{ea} \text{ and } \Phi_h = E_{ip} - W \quad (2)$$

where W is the work function of the metal, and E_{ea} and E_{ip} are the electron affinity and ionization potential of the semiconductor, respectively. $E_{ip} - E_{ea}$ = band gap. These quantities are the intrinsic properties of isolated materials before they form the junction. The Schottky-Mott model suggests that Φ_e (or Φ_h) is linearly dependent on the W of metals with a slope of ±1. However, in reality, Φ is usually insensitive to W, and the FL of the system is pinned to a fixed position in the semiconductor band gap, varying little with respect to the different metals used. The strength of FLP for a given semiconductor with a set of metals can be characterized by the linearly fitted slope of the Φ-versus-W plot (*2*)

$$S = |d\Phi/dW| \quad (3)$$

If S = 1, the Schottky-Mott limit is recovered. Unfortunately, S is small for 3D metal–2D semiconductor junctions. Experiments measured S = 0.1 for 3D metal–MoS_2 junctions (*8*), indicating a strong FLP.

In general, there exist many different models for explaining FLP [see the study by Tung (*2*) for a review], and no simple equations are applicable for all types of MSJs (*2*). Here, we focus on those that have been recognized to be relevant to 2D semiconductors. (i) Metal-induced gap states (MIGS) are formed in the semiconductor (*9*–*12*), as also observed in many 3D metal–3D semiconductor junctions (*2*, *13*–*19*). These states serve as a reservoir for electrons or holes and therefore pin the FL. (ii) An interface dipole formed by the charge redistribution at the interface can shift the electronic levels from their original positions, leading to a deviation from the Schottky-Mott limit (*2*, *9*, *20*, *21*). (iii) Defects at the interface (created during material/device fabrication) could generate gap states that pin the FL (*1*, *2*, *22*), yet this can be neglected for a high-quality interface.

Here, we show that contrary to the conventional 3D metal–2D semiconductor junctions, FLP is weak for the MSJ formed by van der Waals (vdW) interactions, which is attributed to the suppression of MIGS in the semiconductor. This phenomenon allows for the tuning of Φ by using different 2D metals. On this basis, we identify the promising 2D metals that can form a low-Φ junction with 2D semiconductors.

[1]National Renewable Energy Laboratory, Golden, CO 80401, USA. [2]Beijing Computational Science Research Center, Beijing 100094, China.
*Corresponding author. E-mail: yuanyue.liu.microman@gmail.com (Y.L.); suhuaiwei@csrc.ac.cn (S.-H.W.)
†Present address: California Institute of Technology, Pasadena, CA 91125, USA.

RESULTS

We consider a wide range of 2D metals that have been experimentally realized, including the following: (i) triangular (*T*) and distorted triangular (*T*′) phases of MoX_2 and WX_2; (ii) group 5 MX_2 (M = V, Nb, or Ta) and TiX_2, which exhibit either hexagonal (*H*) or *T* phase at room temperature; and (iii) pristine and doped graphene. These materials have chemically saturated surfaces and bind with 2D semiconductors through vdW interactions.

Figure 1A shows a typical band structure of a 2D MSJ by using *T*-MoS_2–*H*-MoS_2 as an example (*T*-MoS_2 is a metal and *H*-MoS_2 is a semiconductor; see computational details in the Supplementary Materials). The origin of each electronic state can be determined from its charge density distribution, based on which we identify the VBM and the CBM of the semiconductor in the junction (as marked by the blue and red dots, respectively, in Fig. 1A). We then plot the distribution of the states between the VBM and the CBM in the junction (Fig. 1A) and find that these states come from the metal rather than the semiconductor. Therefore, the MIGS in the semiconductor of the junction are negligible, which is further evidenced by projecting density of states (DOS) onto the semiconductor (Fig. 1A). This feature is in contrast to 3D metal–2D semiconductor junctions, where MIGS are significant (*9*–*12*). We attribute this phenomenon to the unique interaction between the metal and the semiconductor at the vdW MSJ, which is substantially weaker than the chemical bonding in other junctions (*9*, *12*). Indeed, our calculations show that the distance between the 2D metal and the 2D semiconductor falls within 3 to 4 Å (depending on the computational methods and materials), a typical distance for vdW interactions. It is interesting to notice that the interaction can also be weakened by inserting a thin layer between the metal and the semiconductor to break their direct chemical bond (*23*–*25*). However, in these cases, a proper separation material has to be chosen first. This need is avoided in our case, which also simplifies device fabrication.

The suppression of MIGS in the semiconductor can therefore lead to a weak FLP. To verify, Fig. 1B shows the Φ value (calculated by using Eq. 1) for *H*-MoS_2 with various 2D metals. We choose to study *T*-MoS_2, *T*-WS_2, *H*-VS_2, and *T*-VS_2 because of their small lattice mismatch (<2%) with *H*-MoS_2, which makes the computations efficient. Graphene (though strictly speaking a semimetal) is also selected because it has been used experimentally as an electrode for *H*-MoS_2 (*26*–*30*) (though a large supercell with commensurate structure is required for modeling; see fig. S1 for the structure model; commensurate structures are also used for other largely lattice-mismatched junctions, as shown later). Notably, we find that Φ largely follows the trend of the Schottky-Mott limit (the diagonal line), and its value can vary in a wide range, allowing the tuning of Φ by using different 2D metals. Although different computational methods (more specifically, density functionals) yield different *S* values, they all give *S* values higher than that of 3D metal–*H*-MoS_2 junctions (see figs. S2 and S3 and related text in the Supplementary Materials), indicating a weaker FLP.

Although the vdW interaction is weak, it can redistribute the charge density at the interface and give rise to an interface dipole at the MSJ. This is shown in Fig. 1C, where the charge density (ρ) change after the formation of the junction is calculated for the example for *H*-VS_2–*H*-MoS_2

$$\Delta\rho = \rho(\text{junction}) - \rho(\text{metal}) - \rho(\text{semiconductor}) \quad (4)$$

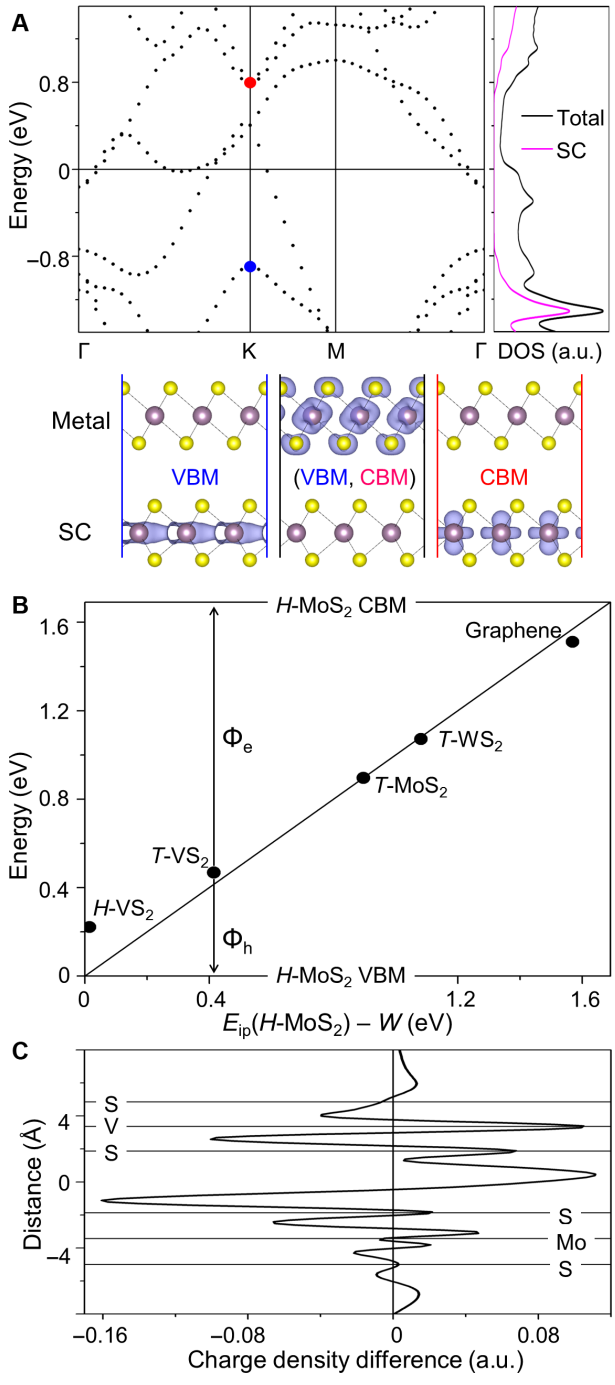

Fig. 1. Weak FLP at the vdW MSJ. (**A**) Electronic band structure and DOS of a typical vdW MSJ. *T*-MoS_2–*H*-MoS_2 is used here as an example, where *T*-MoS_2 is a metal and *H*-MoS_2 is a semiconductor (SC). FL is set to zero. The VBM and CBM of the SC are marked by blue and red dots, respectively. The purple line shows the DOS projected on the semiconductor. Isosurfaces show the spatial distributions of the states. (**B**) SB heights (Φ_e for electrons and Φ_h for holes) between *H*-MoS_2 and various 2D metals. The diagonal line shows the values predicted by the Schottky-Mott model. (**C**) Charge density change (averaged in the plane parallel to the interface) after the formation of the *H*-VS_2–*H*-MoS_2 MSJ. Atom positions perpendicular to the basal plane are shown as distances relative to the center of the interface and marked by horizontal lines. a.u., arbitrary units.

We find an asymmetric charge accumulation/depletion across the interface, indicating the formation of an interface dipole. As discussed above, this interface dipole can shift the electronic levels from their original positions, leading to a deviation from the Schottky-Mott limit (*2*, *9*, *20*, *21*).

Because FLP is weak for the vdW junction, Φ_h (or Φ_e) can be effectively reduced by using high-*W* (or low-*W*) metals as electrodes.

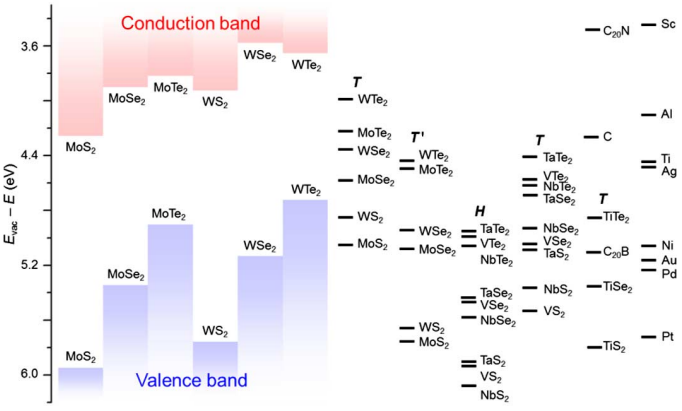

Fig. 2. Band alignment between 2D metals and semiconductors. Left columns show the electron affinity and ionization potential of semiconductors. Right bars show the work function of metals. The phase is labeled in italics. C stands for pristine graphene, $C_{20}N$ is the N-doped graphene with the C/N ratio of 20:1, and similarly for $C_{20}B$. For comparison, the work functions of some commonly used 3D metals are also shown.

To identify the promising candidates, we calculate the *W* of various 2D metals and compare them with the E_{ip} and E_{ea} values of 2D semiconductors, as shown in Fig. 2. These energies show a systematic variation as the cation or anion changes.

For 2D semiconductors, we find that (i) as the atomic number of X increases (from S to Se to Te), the CBM and VBM energies increase (except that the CBM of WTe_2 is lower than that of WSe_2) and band gap decreases; and (ii) moreover, for the common X system, the CBM and the VBM energies of WX_2 are higher than those of MoX_2. These observations agree with literature results calculated using different methods (*31*, *32*). Therefore, MoS_2 has the lowest CBM and VBM, WTe_2 has the highest VBM, and WSe_2 has the highest CBM. These results explain why MoS_2 is usually n-type in experiments but WSe_2 is p-type: compared with MoS_2, WSe_2 has higher CBM and VBM and therefore has higher Φ_e but lower Φ_h for given metals, resulting in easier hole injection but more difficult electron injection (*33*).

For 2D metals, we find that (i) for the same M, the *W* of MX_2 increases as the X atomic number decreases, and (ii) for the same X, the *W* of MX_2 increases as the M atomic number (in the same group) decreases (except for VX_2, which is magnetic, in which case the spin polarization changes the order between VX_2 and NbX_2). These trends originate from the coupling between the M *d* orbitals and the X *p* orbitals. As shown by the projected DOS (Fig. 3A), the states near the FL are contributed by the M *d* states and X *p* states, and their spatial distribution suggests that they are antibonding-coupled (Fig. 3B). For common M systems, because M *d* states have higher energy than X *p* states (*31*) (Fig. 3C), the *p*-*d* coupling weakens and the repulsion level reduces as the *p* energy decreases from Te to Se to S. This decreases the energy of the antibonding states, and thus the FL moves down and *W* increases.

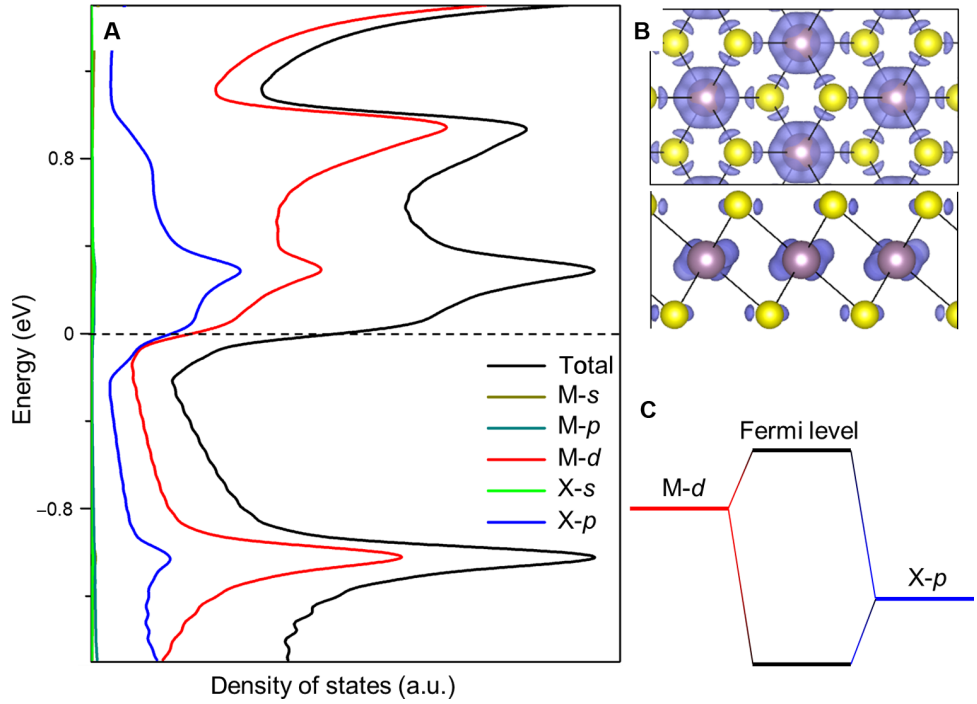

Fig. 3. Origin of work function variation in 2D metals. (**A**) DOS of metallic MX_2 (*T*-MoS_2 is used here as an example). FL is set to zero. The black line shows the total DOS, and the other lines are the projected DOS on the orbitals of M and X. (**B**) Charge density distribution of the states in the electron volt range (−0.025, 0.025) (top and side views). (**C**) Schematic of coupling between M *d* states and X *p* states.

For common X systems, the M *d* energy decreases, and the Coulomb repulsion between the *d* electrons increases when M moves up in the same group (*34*); thus, the FL decreases and *W* increases. We also find that for different phases of MX_2, the FL decreases as the stability increases. For example, *T*′-MoX_2 and WX_2 are more stable than the corresponding *T* phases (*35*) and have lower FLs; the situation is similar for group 5 *H*-MX_2 compared with their *T* phases. Notably, we find that some of the metallic MX_2 (group 5 *H*-MX_2 and TiS_2) have higher *W* than Pt, which has the highest *W* among elemental metals. Of these, *H*-NbS_2 has the highest *W*, suggesting that it could be a promising electrode for achieving low-Φ_h contact with the semiconductor, as shown later.

We also explore the potential of using doped graphene as electrodes. B has fewer electrons than C, thus B doping increases the *W* of graphene; inversely, N has more electrons than C, and its doping decreases the *W* of graphene. In particular, at a high N-doping concentration (C/N, 20:1), *W* is as low as that of Sc and below all 2D MX_2 metals, implying that it could be a promising electrode for electron injection.

After identifying the promising metal electrodes based on their *W*, we calculate their Φ with the 2D semiconductors, as shown in Fig. 4 (see fig. S4 for representative band structures and table S1 for a comparison of the results calculated with different methods). Indeed, *H*-NbS_2 can form a low-Φ_h junction. In particular, Φ_h is negative when *H*-NbS_2 contacts *H*-WTe_2, $MoTe_2$, WSe_2, or $MoSe_2$, indicating a spontaneous electron transfer to *H*-NbS_2 and a hole injection into the semiconductor upon contact. Note that this strong charge transfer shifts the FL and the VBM from their original positions, leading to a deviation from the ideal Schottky-Mott model. Similarly, $C_{20}N$ can form a low-Φ_e contact. However, as opposed to *H*-NbS_2, which has been experimentally synthesized, an efficient N-doping approach up to high concentrations has yet to be developed.

DISCUSSION

Using a 2D metal as an electrode has other benefits. First, its transparency and flexibility are compatible with similar features of the 2D semiconductor channel, and it can be integrated for transparent and flexible electronics (*28*, *30*). Second, a 2D metal has limited electronic DOS, and therefore low quantum capacitance. Thus, when charge is accumulated by applying a dielectric-mediated voltage, its *W* changes markedly compared with conventional metals, which have high DOS. This unique feature of a 2D metal leads to a gate-tunable *W* and therefore Φ, as has been observed in experiments (*26*, *36*–*39*). Third, it has been shown that a flat interface between the metal and the semiconductor could facilitate carrier transport (*40*). The atomically flat interface is difficult to achieve by using conventional metals but can be easily realized at the vdW contact. In addition, using a 2D metal as an electrode allows full encapsulation of the semiconductor, which prevents contamination from the environment (*29*, *39*) or stabilizes the reactive semiconductor such as phosphorene (*41*). Moreover, suppression of MIGS reduces the electron-hole recombination at the interface, leading to a higher energy conversion efficiency for optoelectronic devices.

Although this work focuses on the vdW junction, the band alignment shown in Fig. 2 could also provide guidelines for designing a low-resistance "edge" contact junction, where 2D metals and semiconductors are chemically bonded in the same basal plane (*42*). In addition, Fig. 2 also offers guidelines for designing photovoltaic cells based on 2D materials; in this case, it is critical to select electrodes with an FL close to the VBM or CBM of the semiconductor to obtain a high open-circuit voltage.

We discuss several practical issues for NbS_2, which is predicted to be the most promising electrode. In reality, it is easier to obtain a few-layer material than a monolayer; hence, it is interesting to investigate how the electronic structure changes as a function of thickness [we use 3R stacking for multilayer calculations because it is the most common one for NbS_2 (*43*); note that "3R" only denotes the interlayer stacking pattern, and each layer still has the same structure as the monolayer considered above, that is, *H*-NbS_2]. We find that NbS_2 remains metallic independent of the thickness, in agreement with calculations in the literature (*44*). A recent experimental study shows that, in contrast to bulk NbS_2, which is a metal, thin NbS_2 nanoflakes demonstrate semiconducting properties; this is attributed to the presence of surface defects and/or the nonstoichiometry of the samples that can trap the electrons and quench the carriers (*43*). The activation energy is found to be very small (1.4 to 1.5 meV) (*43*). This suggests that it is possible to recover the metallic nature of thin NbS_2 by improving the sample quality. We also find that the difference between the *W* of a monolayer and that of a few-layer (or bulk) material is small (tens

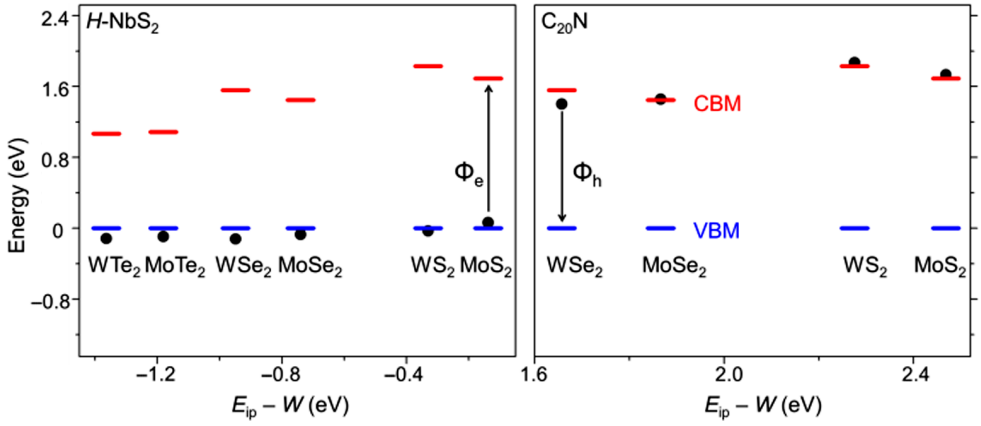

Fig. 4. SB heights for *H*-NbS_2 and $C_{20}N$ metals, with various 2D semiconductors. $C_{20}N$ with tellurides are not calculated because of the extremely large supercell required for modeling to reduce the lattice mismatch. The red bars indicate the CBM, the blue bars represent the VBM that are set to zero, and the black dots denote the position of FL in the corresponding MSJ.

of millielectron volts). Therefore, the low Φ_h should be expected for multilayer NbS_2 as well. Note that Φ would be further lowered by the image charge effect (*1*) when the carriers approach the MSJ during the device operation. The 2D metals may be subject to oxidation when directly exposed to ambient air. This can be overcome by using encapsulation techniques (for example, seal the device with BN) (*29*, *39*, *41*), which have been used to stabilize reactive 2D materials such as black phosphorus (which otherwise would quickly degrade in air) (*41*).

Notice that a recent experimental study shows the presence of interface states at the bilayer-monolayer lateral heterojunction (*45*), which would trap/scatter the charge carriers transporting along the basal plane. However, these would not affect the carrier injection, which occurs at the bilayer region away from the bilayer-monolayer interface. Finally, we notice a very recent experimental study demonstrating that a low contact resistance for hole transport is achieved by using Nb-doped 2D WSe_2 or MoS_2 as contact material (*46*). This further supports our prediction that NbS_2 would be a promising candidate.

In summary, a large and untunable SB is overcome by replacing conventional metals with 2D metals, which form a vdW MSJ with 2D semiconductors. This type of MSJ exhibits a weak FLP, which is attributed to the suppression of MIGS. This work not only advances the understanding of fundamental properties of heterojunctions but also shows novel functions of 2D metals in device applications.

MATERIALS AND METHODS

Figures in the main text were obtained by using density functional theory with projector-augmented wave pseudopotentials (*47*, *48*) and the Perdew-Burke-Ernzerhof (PBE) exchange-correlation functional (*49*), as implemented in the Vienna ab initio simulation package (*50*, *51*). We also used a local-density approximation functional (*52*), as well as PBE with vdW corrections (D3) (*53*), in certain cases to check the robustness of the conclusions, as shown in the Supplementary Materials. Monkhorst-Pack sampling (*54*) of sufficient k-points was used. The vacuum distance between periodic images was kept to >15 Å. All of the structures were relaxed until the final force on each atom was <0.01 eV/Å. E_{ea}, E_{ip}, and W were calculated by subtracting the corresponding electronic levels with respect to the vacuum level in the supercell.

SUPPLEMENTARY MATERIALS

Supplementary material for this article is available at http://advances.sciencemag.org/cgi/content/full/2/4/e1600069/DC1

fig. S1. Supercell used for modeling the graphene–*H*-MoS_2 junction.
fig. S2. Comparison of pinning factor between vdW and chemically bonded junctions.
fig. S3. Φ between 2D *H*-MoS_2 and various 2D metals calculated by using the PBE-D3 method.
fig. S4. Band structure of *H*-NbS_2–*H*-WSe_2 and $C_{20}N$–*H*-MoS_2 junctions.
table S1. Comparison of Φ between the PBE and the PBE-D3 methods.

REFERENCES AND NOTES

1. S. M. Sze, *Physics of Semiconductor Devices* (John Wiley & Sons, New Jersey, 1981).
2. R. T. Tung, The physics and chemistry of the Schottky barrier height. *Appl. Phys. Rev.* **1**, 011304 (2014).
3. Q. H. Wang, K. Kalantar-Zadeh, A. Kis, J. N. Coleman, M. S. Strano, Electronics and optoelectronics of two-dimensional transition metal dichalcogenides. *Nat. Nanotechnol.* **7**, 699–712 (2012).
4. G. Fiori, F. Bonaccorso, G. Iannaccone, T. Palacios, D. Neumaier, A. Seabaugh, S. K. Banerjee, L. Colombo, Electronics based on two-dimensional materials. *Nat. Nanotechnol.* **9**, 768–779 (2014).
5. D. Akinwande, N. Petrone, J. Hone, Two-dimensional flexible nanoelectronics. *Nat. Commun.* **5**, 5678 (2014).
6. D. Jena, K. Banerjee, G. H. Xing, 2D crystal semiconductors: Intimate contacts. *Nat. Mater.* **13**, 1076–1078 (2014).
7. A. Allain, J. Kang, K. Banerjee, A. Kis, Electrical contacts to two-dimensional semiconductors. *Nat. Mater.* **14**, 1195–1205 (2015).
8. S. Das, H.-Y. Chen, A. V. Penumatcha, J. Appenzeller, High performance multilayer MoS_2 transistors with scandium contacts. *Nano Lett.* **13**, 100–105 (2013).
9. C. Gong, L. Colombo, R. M. Wallace, K. Cho, The unusual mechanism of partial Fermi level pinning at metal–MoS_2 interfaces. *Nano Lett.* **14**, 1714–1720 (2014).
10. Y. Guo, D. Liu, J. Robertson, 3D behavior of Schottky barriers of 2D transition-metal dichalcogenides. *ACS Appl. Mater. Interfaces* **7**, 25709–25715 (2015).
11. J. Kang, W. Liu, D. Sarkar, D. Jena, K. Banerjee, Computational study of metal contacts to monolayer transition-metal dichalcogenide semiconductors. *Phys. Rev. X* **4**, 031005 (2014).
12. I. Popov, G. Seifert, D. Tománek, Designing electrical contacts to MoS_2 monolayers: A computational study. *Phys. Rev. Lett.* **108**, 156802 (2012).
13. V. Heine, Theory of surface states. *Phys. Rev.* **138**, A1689–A1696 (1965).
14. S. G. Louie, M. L. Cohen, Self-consistent pseudopotential calculation for a metal-semiconductor interface. *Phys. Rev. Lett.* **35**, 866–869 (1975).
15. S. G. Louie, J. R. Chelikowsky, M. L. Cohen, Ionicity and the theory of Schottky barriers. *Phys. Rev. B* **15**, 2154–2162 (1977).
16. J. Tersoff, Schottky barrier heights and the continuum of gap states. *Phys. Rev. Lett.* **52**, 465–468 (1984).
17. T. Nishimura, K. Kita, A. Toriumi, Evidence for strong Fermi-level pinning due to metal-induced gap states at metal/germanium interface. *Appl. Phys. Lett.* **91**, 123123 (2007).
18. T. C. G. Reusch, M. Wenderoth, L. Winking, N. Quaas, R. G. Ulbrich, Origin of Schottky barriers in gold contacts on GaAs (110). *Phys. Rev. Lett.* **93**, 206801 (2004).
19. D. Çakır, F. M. Peeters, Dependence of the electronic and transport properties of metal-$MoSe_2$ interfaces on contact structures. *Phys. Rev. B* **89**, 245403 (2014).
20. R. T. Tung, Formation of an electric dipole at metal-semiconductor interfaces. *Phys. Rev. B* **64**, 205310 (2001).
21. T. Iffländer, S. Rolf-Pissarczyk, L. Winking, R. G. Ulbrich, A. Al-Zubi, S. Blügel, M. Wenderoth, Local density of states at metal-semiconductor interfaces: An atomic scale study. *Phys. Rev. Lett.* **114**, 146804 (2015).
22. Y. Liu, P. Stradins, S.-H. Wei, Air passivation of chalcogen vacancies in two-dimensional semiconductors. *Angew. Chem. Int. Ed.* **128**, 977–980 (2016).
23. M. Farmanbar, G. Brocks, Controlling the Schottky barrier at MoS_2/metal contacts by inserting a BN monolayer. *Phys. Rev. B* **91**, 161304(R) (2015).
24. D. Connelly, C. Faulkner, P. A. Clifton, D. E. Grupp, Fermi-level depinning for low-barrier Schottky source/drain transistors. *Appl. Phys. Lett.* **88**, 012105 (2006).
25. D. Çakr, C. Sevik, F. M. Peeters, Engineering electronic properties of metal–$MoSe_2$ interfaces using self-assembled monolayers. *J. Mater. Chem. C* **2**, 9842–9849 (2014).
26. L. Yu, Y.-H. Lee, X. Ling, E. J. G. Santos, Y. C. Shin, Y. Lin, M. Dubey, E. Kaxiras, J. Kong, H. Wang, T. Palacios, Graphene/MoS_2 hybrid technology for large-scale two-dimensional electronics. *Nano Lett.* **14**, 3055–3063 (2014).
27. T. Roy, M. Tosun, J. S. Kang, A. B. Sachid, S. B. Desai, M. Hettick, C. C. Hu, A. Javey, Field-effect transistors built from all two-dimensional material components. *ACS Nano* **8**, 6259–6264 (2014).
28. S. Das, R. Gulotty, A. V. Sumant, A. Roelofs, All two-dimensional, flexible, transparent, and thinnest thin film transistor. *Nano Lett.* **14**, 2861–2866 (2014).
29. X. Cui, G.-H. Lee, Y. D. Kim, G. Arefe, P. Y. Huang, C.-H. Lee, D. A. Chenet, X. Zhang, L. Wang, F. Ye, F. Pizzocchero, B. S. Jessen, K. Watanabe, T. Taniguchi, D. A. Muller, T. Low, P. Kim, J. Hone, Multi-terminal electrical transport measurements of molybdenum MoS_2 using van der Waals heterostructure device platform. *Nat. Nanotechnol.* **10**, 534–540 (2015).
30. G.-H. Lee, Y.-J. Yu, X. Cui, N. Petrone, C.-H. Lee, M. S. Choi, D.-Y. Lee, C. Lee, W. J. Yoo, K. Watanabe, T. Taniguchi, C. Nuckolls, P. Kim, J. Hone, Flexible and transparent MoS_2 field-effect transistors on hexagonal boron nitride-graphene heterostructures. *ACS Nano* **7**, 7931–7936 (2013).
31. J. Kang, S. Tongay, J. Zhou, J. Li, J. Wu, Band offsets and heterostructures of two-dimensional semiconductors. *Appl. Phys. Lett.* **102**, 012111 (2013).
32. Y. Liang, S. Huang, R. Soklaski, L. Yang, Quasiparticle band-edge energy and band offsets of monolayer of molybdenum and tungsten chalcogenides. *Appl. Phys. Lett.* **103**, 042106 (2013).
33. S. B. Zhang, S.-H. Wei, A. Zunger, A phenomenological model for systematization and prediction of doping limits in II–VI and I–III–VI_2 compounds. *J. Appl. Phys.* **83**, 3192–3196 (1998).
34. W.-J. Yin, H. Tang, S.-H. Wei, M. M. Al-Jassim, J. Turner, Y. Yan, Band structure engineering of semiconductors for enhanced photoelectrochemical water splitting: The case of TiO_2. *Phys. Rev. B* **82**, 045106 (2010).

35. K.-A. N. Duerloo, Y. Li, E. J. Reed, Structural phase transitions in two-dimensional Mo- and W-dichalcogenide monolayers. *Nat. Commun.* **5**, 4214 (2014).
36. Y.-J. Yu, Y. Zhao, S. Ryu, L. E. Brus, K. S. Kim, P. Kim, Tuning the graphene work function by electric field effect. *Nano Lett.* **9**, 3430–3434 (2009).
37. C.-J. Shih, Q. H. Wang, Y. Son, Z. Jin, D. Blankschtein, M. S. Strano, Tuning on–off current ratio and field-effect mobility in a MoS_2–graphene heterostructure via Schottky barrier modulation. *ACS Nano* **8**, 5790–5798 (2014).
38. H. Tian, Z. Tan, C. Wu, X. Wang, M. A. Mohammad, D. Xie, Y. Yang, J. Wang, L.-J. Li, J. Xu, T.-L. Ren, Novel field-effect Schottky barrier transistors based on graphene-MoS_2 heterojunctions. *Sci. Rep.* **4**, 5951 (2014).
39. Y. Liu, H. Wu, H.-C. Cheng, S. Yang, E. Zhu, Q. He, M. Ding, D. Li, J. Guo, N. O. Weiss, Y. Huang, X. Duan, Toward barrier free contact to molybdenum disulfide using graphene electrodes. *Nano Lett.* **15**, 3030–3034 (2015).
40. H. Yuan, G. Cheng, L. You, H. Li, H. Zhu, W. Li, J. J. Kopanski, Y. S. Obeng, A. R. H. Walker, D. J. Gundlach, C. A. Richter, D. E. Ioannou, Q. Li, Influence of metal–MoS_2 interface on MoS_2 transistor performance: Comparison of Ag and Ti contacts. *ACS Appl. Mater. Interfaces* **7**, 1180–1187 (2015).
41. A. Avsar, I. J. Vera-Marun, J. Y. Tan, K. Watanabe, T. Taniguchi, A. H. Castro Neto, B. Özyilmaz, Air-stable transport in graphene-contacted, fully encapsulated ultrathin black phosphorus-based field-effect transistors. *ACS Nano* **9**, 4138–4145 (2015).
42. R. Kappera, D. Voiry, S. E. Yalcin, B. Branch, G. Gupta, A. D. Mohite, M. Chhowalla, Phase-engineered low-resistance contacts for ultrathin MoS_2 transistors. *Nat. Mater.* **13**, 1128–1134 (2014).
43. Y. H. Huang, C. C. Peng, R. S. Chen, Y. S. Huang, C. H. Ho, Transport properties in semiconducting NbS_2 nanoflakes. *Appl. Phys. Lett.* **105**, 093106 (2014).
44. A. Kuc, N. Zibouche, T. Heine, Influence of quantum confinement on the electronic structure of the transition metal sulfide TS_2. *Phys. Rev. B* **83**, 245213 (2011).
45. C. Zhang, Y. Chen, J.-K. Huang, X. Wu, L.-J. Li, W. Yao, J. Tersoff, C.-K. Shih, Visualizing band offsets and edge states in bilayer–monolayer transition metal dichalcogenides lateral heterojunction. *Nat. Commun.* **7**, 10349 (2016).
46. H. J. Chuang, B. Chamlagain, M. Koehler, M. M. Perera, J. Yan, D. Mandrus, D. Tománek, Z. Zhou, Low-resistance 2D/2D ohmic contacts: A universal approach to high-performance WSe_2, MoS_2, and $MoSe_2$ transistors. *Nano Lett.* **16**, 1896–1902 (2016).
47. P. E. Blöchl, Projector augmented-wave method. *Phys. Rev. B* **50**, 17953–17979 (1994).
48. G. Kresse, D. Joubert, From ultrasoft pseudopotentials to the projector augmented-wave method. *Phys. Rev. B* **59**, 1758–1775 (1999).
49. J. P. Perdew, K. Burke, M. Ernzerhof, Generalized gradient approximation made simple. *Phys. Rev. Lett.* **77**, 3865–3868 (1996).
50. G. Kresse, J. Furthmüller, Efficient iterative schemes for ab initio total-energy calculations using a plane-wave basis set. *Phys. Rev. B* **54**, 11169–11186 (1996).
51. G. Kresse, J. Hafner, Ab initio molecular dynamics for liquid metals. *Phys. Rev. B* **47**, 558–561 (1993).
52. D. M. Ceperley, B. J. Alder, Ground state of the electron gas by a stochastic method. *Phys. Rev. Lett.* **45**, 566–569 (1980).
53. S. Grimme, J. Antony, S. Ehrlich, H. Krieg, A consistent and accurate *ab initio* parametrization of density functional dispersion correction (DFT-D) for the 94 elements H-Pu. *J. Chem. Phys.* **132**, 154104 (2010).
54. H. J. Monkhorst, J. D. Pack, Special points for Brillouin-zone integrations. *Phys. Rev. B* **13**, 5188–5192 (1976).

Acknowledgments: Y. L. acknowledges discussions with B. Yakobson and B. Wood on NbS_2. **Funding:** This research was funded by the U.S. Department of Energy (DOE) under contract no. DE-AC36-08GO28308 with the National Renewable Energy Laboratory (NREL) and supported by the DOE Energy Efficiency and Renewable Energy (EERE) DE-261 EE0006336 FPACE-II. This work used computational resources at the NREL (sponsored by the DOE EERE) and the National Energy Research Scientific Computing Center (supported by DOE Office of Science DE-AC02-05CH11231). **Author contributions:** Y. L. conceived the idea and performed the calculations. Y. L., P. S., and S.-H.W. analyzed the data. Y. L. and S.-H.W. wrote the paper. **Competing interests:** The authors declare that they have no competing interests. **Data and materials availability:** All data needed to evaluate the conclusions in the paper are present in the paper and/or the Supplementary Materials. Additional data related to this paper may be requested from the authors.

Submitted 15 January 2016
Accepted 24 March 2016
Published 22 April 2016
10.1126/sciadv.1600069

Citation: Y. Liu, P. Stradins, S.-H. Wei, Van der Waals metal-semiconductor junction: Weak Fermi level pinning enables effective tuning of Schottky barrier. *Sci. Adv.* **2**, e1600069 (2016).

ScienceAdvances
AAAS

Van der Waals metal-semiconductor junction: Weak Fermi level pinning enables effective tuning of Schottky barrier
Yuanyue Liu, Paul Stradins and Su-Huai Wei (April 22, 2016)
Sci Adv 2016, 2:.
doi: 10.1126/sciadv.1600069